# Ex Situ Endorectal MRI Probe for Prostate Imaging

Aharon Blank,[1*] Shlomo Ish-Shalom,[1] Lazar Shtirberg,[1] and Yuval Zur[2]

A unique ex situ MRI probe, which examines samples external to its geometry, is presented. The probe is intended to be used for imaging the prostate gland via an endorectal pathway. It has a semicylindrical shape with a length of 6 cm and typical diameter of ~3 cm. The probe's imaging field of view spans almost along its entire length and up to a distance of 2 cm away from its surface, with an angular sector of ~90°. The detailed design of the probe is presented, followed by a set of representative results obtained by the current bench prototype of this system. **Magn Reson Med 62:1585–1596, 2009.** © 2009 Wiley-Liss, Inc.

Key words: NMR; MRI; inside-out; ex situ; prostate

NMR and its descendant MRI are usually pursued in a setup based on a highly homogenous static magnetic field, $B_0$, with variance <1 ppm, creating nuclear spin precession at a corresponding narrow band of frequencies (1). The homogeneous static field setup has several advantages, such as the ability to obtain chemical shifts while ensuring good signal-to-noise ratio (SNR) due to the small bandwidth involved. However, this setup suffers from the need to employ large magnets that usually surround the examined sample/object. In specific cases, such as clinical MRI systems, the large magnet, and the corresponding large radiofrequency (RF) and gradient coils, are a major factor in the relative complexity and the high cost of such systems. If one is interested only in a specific small region within the body, it could be highly advantageous to obtain NMR information by using either a noninvasive handheld probe or an intracavity self-contained (magnet + RF and gradient coils) NMR probe, thus avoiding the requirement for a large external magnet. Such an approach to NMR measurement or NMR imaging without a sample-surrounding magnet is termed "inside-out," or ex situ (2-6). In the "inside-out" setup it is very difficult to create highly homogeneous fields without making significant compromises regarding field magnitude. Several types of systems that operate in an "inside-out" geometry have been designed and built, demonstrating measurement capabilities of relaxation parameters (7,8), diffusion coefficients (9), spectroscopic data (10), and three-dimensional (3D) imaging (11). In the case of microscopic MRI, where very high field gradients are required to obtain a high resolution, "inside-out" systems were found to be very useful and enabled the acquisition of images with a resolution of 1 μm or better, outside a superconducting magnet (4,12), or near a microscopic magnetic tip (13,14).

The efforts described above were mainly directed toward materials science applications or related subjects, with appreciable achievements. In the field of medicine, recent work has demonstrated the use of a miniature intravascular ex situ NMR probe with one-dimensional imaging capability for the detection of vulnerable plaque in the coronary arteries (15-17). Larger nonimaging and/or one-dimensional imaging probes have been shown to be useful in obtaining interesting clinical results regarding the examination of tendon anisotropy, skin conditions, and breast implants (18). Despite this progress, the "dream" of widely using a set of simple and affordable ex situ NMR/MRI probes for a variety of medical applications is far from being realized. This is mainly due to the fact that while ex situ NMR systems are superior to conventional MRI systems as regards affordability and simplicity, their limited field of view (FOV) and low SNR are not sufficient for most clinical applications. For example, ex situ NMR imaging with a typical ~30-cm-size probe can achieve a slice of a selected two-dimensional image with a resolution of ~[1 mm] (2) for an FOV of ~3 × 3 cm and a penetration depth of up to ~1 cm from the probe surface (11,18). These performances, especially if considered in conjunction with a general-purpose clinical use, are not sufficient. Nevertheless, as was shown in the case of the miniature intravascular probe (15), if one tailors a specific probe design to a very specific clinical application, ex situ NMR/MRI can be a viable solution that complements the current conventional MRI capabilities.

In this paper, we present a design and experimental results for a new application-specific ex situ MRI probe with 3D imaging capability, intended for future use in prostate cancer diagnosis and staging. Prostate cancer is one of the most common types of cancer affecting men in the United States and all over the world. MRI is known to be a powerful methodology in the detection and staging of this disease (19). However, its relatively high complexity and cost prevent it from being a useful tool for applications such as screening, biopsy targeting, and periodic staging. In view of this, we have come up with this new probe that could be used in an endorectal manner, in conjunction with a conventional ultrasound module. The ultrasound device can guide the probe to the location of the prostate and may be also used in conjunction with targeted biopsy, based on a combined ultrasound/MRI image produced by the probe. Here we will describe the design and characteristics of a laboratory prototype of the MRI module, present experimental results for test samples, and discuss the overall probe performance with respect to the clinical requirements. Preliminary "bench"-type experiments confirmed the unique capabilities of the probe, which, following the necessary clinical-related adjustments, may be incorporated in human experiments in the future.

[1]Schulich Faculty of Chemistry, Technion–Israel Institute of Technology, Haifa, Israel

[2]TopSpin Medical (Israel) Ltd., Global Park, Lod, Israel

*Correspondence to: Aharon Blank, PhD, Schulich Faculty of Chemistry, Technion–Israel Institute of Technology, Haifa, 32000, Israel. E-mail: ab359@tx.technion.ac.il
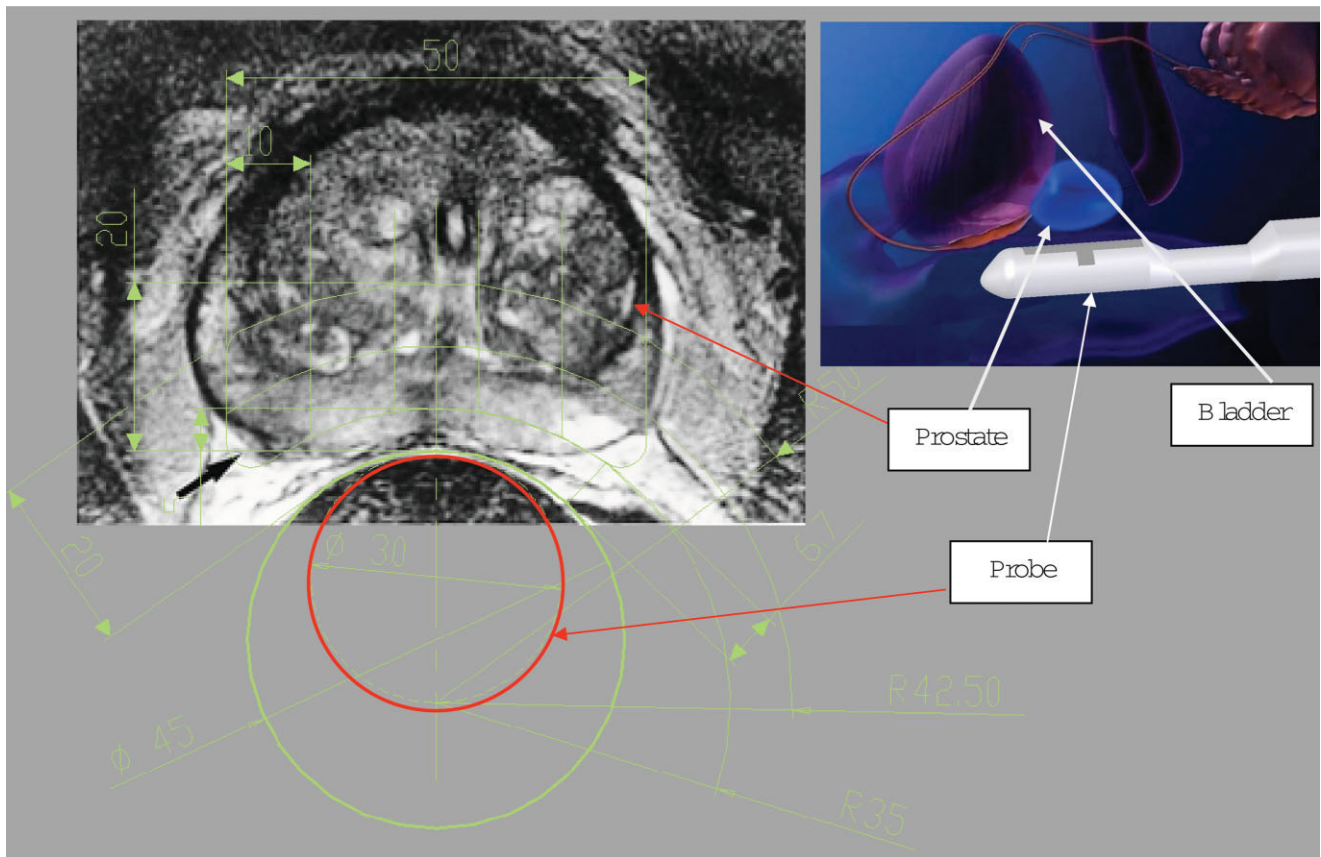
FIG. 1. Conceptual operation scenario for the future endorectal MRI probe. The image shows a cross-section of a typical prostate alongside the probe (marked schematically by a red circle with a diameter of 30 mm), and the rectum void that is schematically represented by a green, 45-mm-diameter circle. A single slice of the probe's FOV is also shown (marked by 10 curved green voxels). It extends up to 20 mm away from the probe surface. Overall, there can be five to 10 such slices extending along the probe's main axis, covering a span of 5 cm.

### Technical Description of the Probe

The main constraint guiding the design of the self-contained MRI probe is that it has to fit inside the rectum and approach the prostate in a manner similar to that of an endorectal ultrasound device or endorectal MRI receiving coil. Figure 1 shows a typical transverse slice image of the prostate, obtained using conventional MRI. The area of the rectum is clearly visible at the bottom of the image, and this is the location to which the endorectal MRI probe should be guided. While the void inside the rectum is relatively large in diameter (~45 mm), we have found that many physicians would agree that a diameter of ~30 mm represents the upper limit of probe size that can be safely inserted into most adult rectums (as confirmed by clinical experiments carried out with a mockup version of the probe). In view of the above, it was decided that the size of the MRI module in the probe should be confined to no more than half of a cylinder; that is, 30 mm in diameter and 60 mm in length (the other half of the probe is reserved for the ultrasound module). In order to achieve sufficient capabilities that will meet at least some of the stringent requirements of the clinical community, this relatively small-sized module was "pushed to the limit" to enable 3D imaging with a FOV of $\sim 15 \times 50 \times 50$ mm that extends up to a distance of 20 mm away from the probe surface and

covers most of the prostate's peripheral zone (Fig. 1). Thus, while such relatively small probe cannot image the entire prostate, it can still observe an important section of it that is known to be the source of most cancer cases. Furthermore, the peripheral zone of the prostate is the main area from which needle biopsy is acquired.

In order to achieve sufficient imaging capabilities while constrained to limited-size cylindrical probe geometry, a variety of unique features had to be incorporated and many challenges had to be overcome. These novelties include a complex magnet design that enables the excitation of concentric arcs near the probe, two-axis imaging gradients sitting on a curved surface with a large FOV, multi-layered transmit and receive coils with electronic frequency tunability in the 2- to 8.5-MHz range having low stray capacitance, shields against magneto-acoustic ringing effects, and an electronic system for the generation of intense/short gradient pulses. The overall structure of the MRI module is shown in Fig. 2. We will proceed now to outline in details the various components of this module, including the main design considerations.

#### Magnet

The first item of the MRI module is the permanent magnet. One of the major limitations of most ex situ probes is the

Back of the probe
(reserved for US module)

Z gradient coils

Magnet

Front of the probe
(sample side)

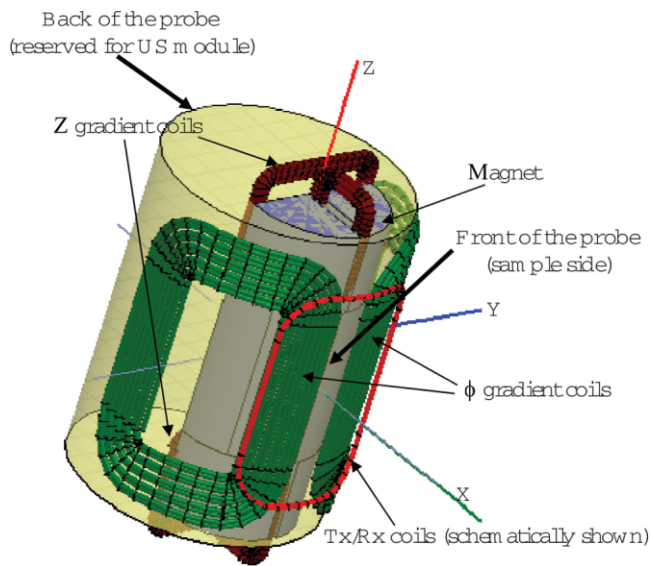φ gradient coils

Tx/Rx coils (schematically shown)

FIG. 2. Mechanical structure of the self-contained MRI module in the endorectal probe. The probe is attached to the side of the rectum (schematically shown by a large yellow cylinder). The origin of the frame of reference of the probe is at the center of the magnet (items will be referred to in this paper by a Cartesian or cylindrical frame of reference, depending on their function in the probe).

relatively small volume of excitation due to a relatively high gradient created outside the magnet. In principle, one can propose an ex situ magnet design that creates a relatively homogenous spot in the required FOV (10,20), but this "sweet spot" would be much smaller than the magnet size, with a relatively low field magnitude. A more ad-

vanced but complex-to-implement design that includes mechanically adjustable magnetic sources can increase the overall homogenous FOV, but this still would be much smaller than the size of the magnet (21). Thus, for limited-sized probes, as the one considered here, when the required FOV is similar to the magnet size, a homogenous design is not practical. In view of that, one of the key considerations regarding the magnet's design was that its equifield lines should coincide with the voxel structure shown in Fig. 1 (see also Fig. 3). In addition, the magnet must allocate enough space for the gradient coils and the ultrasound module in the back of the probe. Furthermore, the magnetic field should be as high as possible, with a relatively high gradient to enable good SNR (due to the relatively high field) and capabilities to acquire images with good diffusion-weighted contrast (due to the relatively high gradient), if required. All these considerations led to the magnet configuration shown in Fig. 3. The magnet is made of NdFeB rare-earth permanent magnet (VACODYM 722 from Vacuumschmelze, Hanau, Germany). It is composed of eight pieces, each magnetized in a different direction (Fig. 3a) to produce the required magnetic field profile. The calculated magnetic field (done with Ansoft finite element software, Ansoft, Pittsburgh, PA) shows good uniformity both along the Z-axis (Fig. 3c) and along the φ-axis (Fig. 3b) of the probe. Static field measurements made with a miniature Hall sensor (model 3RT100-2-2-0.2T; Sentron, Zug, Switzerland) show good correspondence to the calculations (Fig. 3d). It is evident that the field varies from ~0.2 to 0.05 T (8.5-2 MHz) over the entire FOV. The wide variability of the magnetic field over the FOV leads to several challenges that must be faced. These include, for example, a large gradient of ~10

FIG. 3. **a:** Permanent magnet configuration of the MRI module. The overall height of the magnet is 60 mm and its radius is 13.5 mm. The magnet's upper and lower sections are magnetized according to the drawing in angles of ±25° with respect to the Y-axis of the probe (shown by the red arrows in the drawing). In the central part of the magnet, the magnetization direction angles are ±15° with respect to the Y-axis of the probe (shown by the red arrows in the drawing). **b:** Calculated two-dimensional plot of the magnetic field in the XZ plane; **(c)** calculated two-dimensional plot of the magnetic field in the XY plane; **(d)** calculated (solid line) vs measured (red dots) magnetic field along the X-axis of the probe.
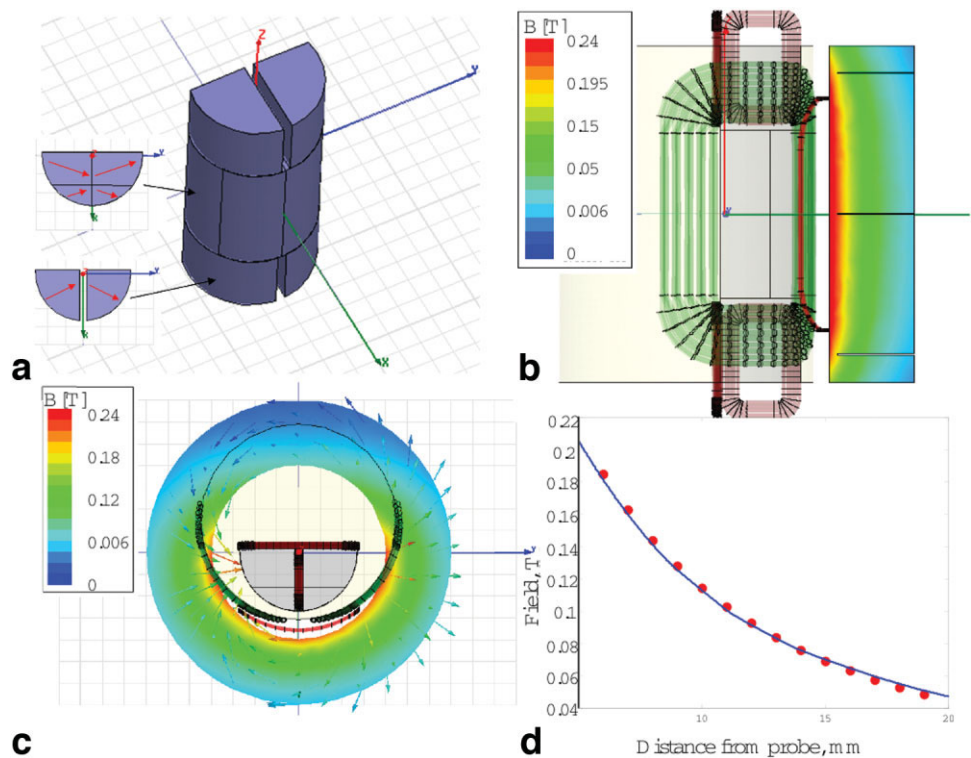
T/m that makes it difficult to excite large volumes instantaneously, and a wide range of operating frequencies that complicates the electronic design of the RF front end, as will be shown in the next subsection. On the other hand, due to the large static gradient of the probe, it is relatively insensitive to temperature changes that can cause drifts of up to ~0.3% per °C in the static magnetic field. In the current type of design, these changes may only lead to negligible variations in the excitation volumes for a given RF frequency (but in a more homogeneous design this would constitute a major problem).

*RF Coils*

Following the description of the design and the construction of the static magnetic field source, we now consider the RF coil configuration. The current probe design incorporates separate transmit and receive coils. Although both coils have the same geometry and are located in the same position in the probe, we have found it necessary to employ two separate coils in order to support the option of electronic tuning of the receive coil over a wide frequency range (see below).

*Transmit coil*. Our probe has a relatively large static field gradient and therefore the transmit (Tx) coil must be optimized to enable excitation of a large volume (covering a large span of resonance frequencies) for a given available RF peak power. In the present design the RF peak power was limited to 2 kW. Higher peak power amplifiers are of course available, but their cost may be prohibitive for our system and, most important, they may induce arcing in the compact Tx coil. An optimal design of the Tx coil should therefore include the following features: (a) the FOV of the RF field produced by the coil should conform with the required FOV of the probe (and the static field source), with RF field direction perpendicular to the static magnetic field and field magnitude that decays as slowly as possible when moving away from the probe surface; (b) the coil's physical structure should minimize the phenomenon of arcing at high transmitted peak power; (c) the quality factor of the coil should match the maximum available excitation bandwidth in view of the power available from the power amplifier; and (d) the resonance frequency of the coil should be easily tuned, preferably electronically, over a wide frequency range of ~2-8.5 MHz.

Let us now consider in more details these design requirements and the manner by which they can be realized. The first requirement is fairly conventional and is realized by the appropriate geometrical design of the coil, as shall be described below (see also Fig. 4b,c). The second and the third requirements are solved by employing a multilayered coil design in which capacitors are distributed between each coil layer (22). With such a design, the reactive voltage generated in each coil section is cancelled by the negative reactive voltage on its adjacent serial capacitor. This kind of structure also makes it possible to obtain an overall coil inductance and a quality factor, for a given coil resistance, that are much higher than that of the usual single coil/capacitor structure. This is because the problem of stray capacitance is greatly reduced with such coil geometry since each coil section is decoupled from its neighbors by its adjacent serial capacitor. The fourth re-

quirement is addressed by the use of a combination of mechanical relay switches and wide band matching transformer, as shall be described in more details below. In view of all that, the Tx coil design has the following characteristics: (a) the coil's geometry is an ellipse with a semimajor axis $a = 18$ mm and a semiminor axis $b = 14$ mm. The coil is bent on a radius of curvature of 22.5 mm, which is slightly larger than the probe radius and mimics a situation where the coil can be expanded during operation to the inner radius of a typical rectum cavity (Fig. 2); (b) the total coil structure is made of four coil subsections, each of which has eight windings of ~0.2-mm-diameter Litz wire (made of 30 wires with 0.02-mm diameter) that withstand 3000 V (Elektrisola, Boscawen, NH); (c) each subsection of the coil has an inductance of 18.8-20 $\mu$H (including the mutual inductance between coil subsections). The total coil inductance, L, is ~77 $\mu$H and its AC resistance, $R_{AC}$, is ~50 $\Omega$, leading to a quality factor, Q, of ~40 (at 4 MHz, the center of the FOV); (d) tuning and matching capacitors are connected between each coil subsection. A set of fast mechanical relays can switch between the values of these capacitors. For example, when operating around 2 MHz we employ capacitors values of 335, 326, 316, and 326 pF to match the four coils' subsections, and for 5 MHz we use the values 37, 36, 35, and 36 pF. Fig. 4a shows the measured current flowing into the Tx coil for the two different positions of the mechanical relays. A matching autotransformer with a turn ratio of 1:4 (where the larger number of turns is attached to the coil) reduces the apparent impedance of the Tx coil by a factor of 16 and this increases the possible instantaneous excitation bandwidth in our configuration by a factor of ~6-8. With this method one can cover the entire bandwidth of interest using only two to four different relay states (depending on the requirements for peak current into the coil and the available RF power). Fig. 4b,c shows the spatial dependence of the RF magnetic field of the Tx coil for 1 A of excitation current. In view of the above, with a drive current of 10 A peak (available from our 2-kW power amplifier), one can generate with this Tx coil pulses with a bandwidth of ~50-250 kHz (for the farthest and closest points in the FOV, respectively).

*Receive coil*. The receive (Rx) coil is identical to the Tx coil in terms of its winding geometry and electrical properties (L and R). The difference between the two is that while the transmit coil is tuned to a certain operating frequency by a combination of mechanical relay switches and a transformer (see above), the receive coil employs a combination of mechanical relay switches and electric tuning of a variable capacitance diode (varactor) to reach the precise operating frequency without a significant reduction in its Q-factor. The varactor-based instantaneous narrow band frequency tuning is much better than using a transformer spoiling Q for wide band matching since it retains the high sensitivity of the coil. However, we have found it very difficult to employ varactor diodes as part of the Tx coil circuit because their capacitance tends to vary as a result of the RF voltage itself during the high power pulses. This observation was the main reason leading to the separation of the Tx and Rx coils. Furthermore, in order to eliminate coupling between the coils, which would induce unwanted voltage on the receiver and the
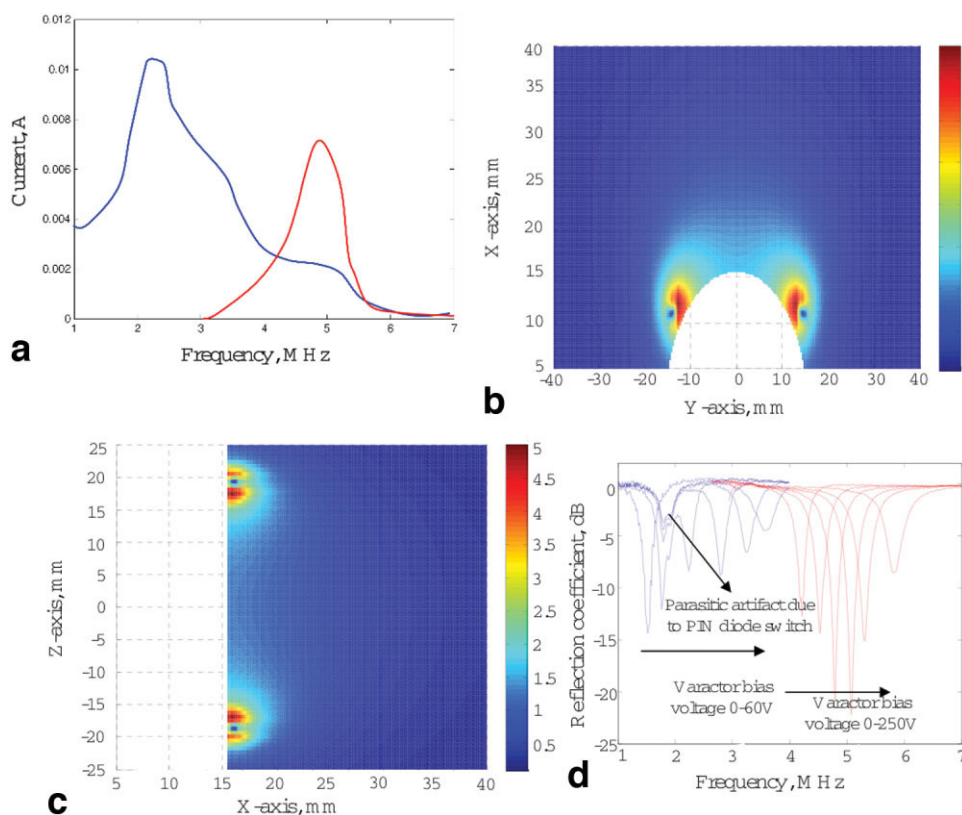
FIG. 4. **a:** Measured current into the Tx coil for 1 V peak excitation as a function of frequency for two different positions of the mechanical relays (switching between capacitor values that correspond to 2 MHz – red, and 5 MHz – blue, see text). **b:** $B_1$ field for excitation current of 1 A in the Tx coil shown for the XY plane of the probe (the origin is at the center of the probe, see Fig. 2). **c:** The same as **(b)** but for the XZ plane. **d:** Measured reflection coefficient of the Rx coil for two sets of fixed capacitor values and a varactor diode (tuned by applying negative voltage bias). For the lower frequencies (blue graphs), we employed capacitor values of 299, 144, 140, and 144 pF in between the four coil subsections, where the fifth capacitor is the varactor with varying capacitance of ~750-130 pF. For the higher frequencies (red graphs), we employed capacitor values of 74, 36, 35, and 36 pF in between the four coil subsections, where the fifth capacitor is the varactor with varying capacitance of ~750-60 pF. The measurements of the reflection coefficient were carried out by means of an RF vector network analyzer (model 6000; Ten-Tec, Sevierville, TN).

varactor during the transmit pulse, the Rx coil is also serially connected to two positive-intrinsic-negative diode switches. The capability of the combined varactor- and relay-based method for tuning the Rx coil is shown in Fig. 4d for two sets of fixed capacitance values (determined by the mechanical relays), and a varying varactor reverse bias voltage (model CREE C2D10120).

*Calculated NMR Signal Without Gradient Coils*

The information about the static field, $B_0$, and the RF field, $B_1$, of the transmit and receive coils and their electrical properties can be compiled with the aid of a 3D NMR simulation (15,23) to extract the theoretical SNR and the geometry of the volume sections around the probe from



FIG. 5. Plots showing the calculated geometry of the excited volumes from which the NMR signal is obtained as appears for the XY **(a)** and XZ **(b)** planes of the probe. The color scale shows the normalized signal obtained from each small volume unit.
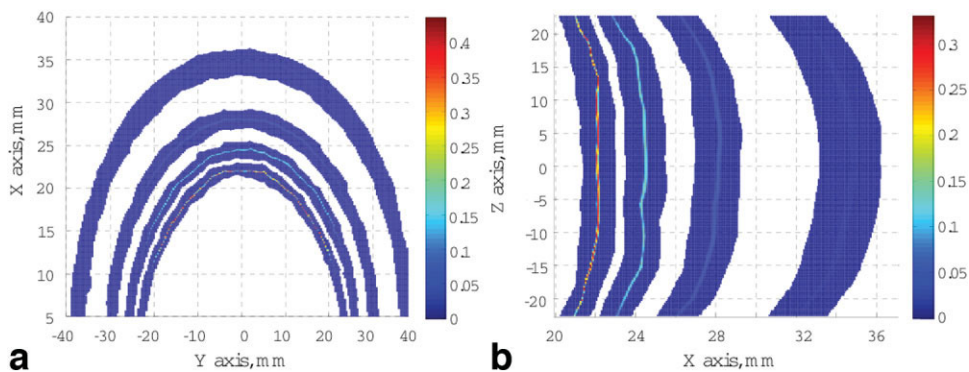
Table 1
Geometrical and NMR Characteristics of the Volume Sections Excited by the Probe at Different Representative Frequencies of Operation

| Freq., MHz | Location, mm[a] | Volume, μL | Width, mm | SNR[b] | Tx current, amp.[c] | φ Gradient, T/m/A | φ Res., mm[d] | Z gradient, T/m/A | Z res., mm[d] |
|---|---|---|---|---|---|---|---|---|---|
| 6.5 | 7.2 | 305 | 0.9 | 4.8 | 2.2 | 0.0119 | 1.0 | 0.0069 | 1.8 |
| 5 | 10 | 497 | 1.3 | 3.2 | 3.2 | 0.0082 | 1.5 | 0.0047 | 2.6 |
| 3.5 | 13.7 | 857 | 1.7 | 1.8 | 4.7 | 0.005 | 2.4 | 0.0029 | 4.2 |
| 2 | 20.6 | 1835 | 2.6 | 0.65 | 9.1 | 0.0022 | 5.6 | 0.0012 | 9.6 |

[a]Location of the center of the excited volume (distance from the probe edge).
[b]Single shot, assuming receiver noise figure of 3 dB.
[c]For 180° pulse.
[d]Resolution along the relevant axis, for a 50-A peak, 30-μs-long half-sine gradient pulse.

which the signal is obtained. Fig. 5 shows the calculated excited volume sections by 100-kHz-pulse Carr-Purcell-Meiboom-Gill (CPMG) echo sequences for the representative frequencies of 2, 3.5, 5, and 6.5 MHz. Table 1 presents some characteristic features of each excited volume section.

*Gradient Coils*

As presented above, the aim of the MRI module is to provide a 3D imaging capability covering a partial cylindrical section outside the probe (Fig. 1). The imaging capability is achieved through the use of φ- and Z-gradients which encode the image along the φ- and Z-cylindrical axes of the probe, while the R-axis is encoded by the constant read gradient of the probe's permanent magnet (Fig. 3d).

φ-*Gradient coils.* The φ-gradient coils are shown schematically in Fig. 2. They comprise two antisymmetric coils that are located at an angle of ±65° with respect to the X-axis of the probe. Each coil is made of 0.7-mm-diameter copper wire, with 28 windings around a $32 \times 16 \times 2$ mm rectangular core. In order to effectively cover the entire FOV, the design of the φ gradient coils requires them to be expandable outward from the probe's inner diameter of 30 mm to a diameter of ~45 mm during operation (which is the typical inner diameter of rectal curvature around the prostate region). The two coils are connected in parallel and have a total inductance of 16.2 μH and resistance of 0.15 Ω. Fig. 6a shows the calculated fields generated by the φ gradient coils along the equifield arcs in the XY plane of

the probe (from which the signal is obtained; see Fig. 5 for the excited volume geometry in the XY plane). It is evident that while the gradient is not constant along the FOV, the fields are still all monotonic functions, which is sufficient to effectively spatially encode the information along the φ axis (see the discussion about imaging sequence below). The average value of the gradient and the image resolution for gradient pulse with a peak current of 50 A and a duration of 30 μs (half-sine shape) are provided in Table 1. Due to the fact that the coils are finite along the Z-axis of the probe, the average gradients become weaker when moving away from the center of the probe (Z = 0) by as much as 28%. These characteristics, which are unavoidable when a relatively large FOV is acquired with a relatively small and curved (cylindrical) probe geometry, can result in severe image artifacts and distortions. They will be considered in more detail in section 4 when we discuss the imaging algorithm and image-correction measures.

*Z-gradient coils.* The Z-gradient coils are shown schematically in Fig. 2. The structure of these coils is based on six single rectangular coils. Each rectangular coil is made of 0.35-mm-diameter copper magnet wire, with 40 windings around a $13.6 \times 7 \times 2$ mm rectangular core. Three coils are positioned on the upper part of the probe and three coils on the lower part of the probe, so that their centers are positioned at positions Z = ±25 mm, as shown in Fig. 2. The three coils on the upper (lower) side of the probe are connected in series. The upper and lower sets of coils are then connected in parallel in an antisymmetric manner and have a total inductance of 22.6 μH and a
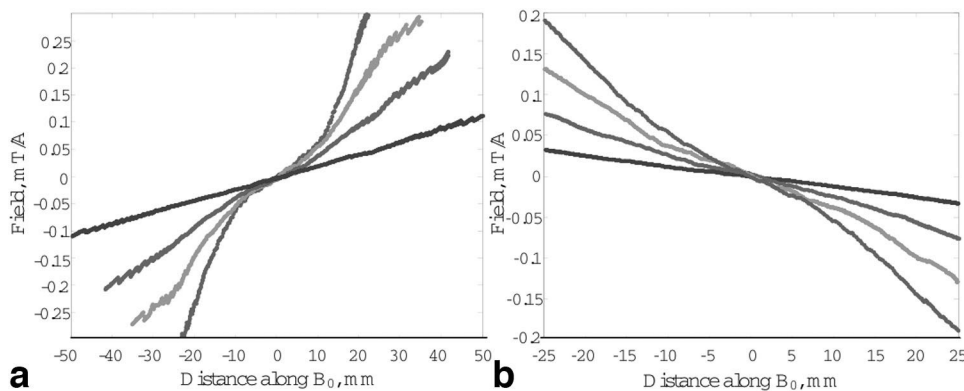
FIG. 6. **a:** Calculated magnetic field generated by the φ-gradient coils with 1 A of current excitation, plotted along equifield lines in the XY plane for the fields 0.047 (blue), 0.0824 (red), 0.1175 (green), and 0.1529 T (magenta) (2, 3.5, 5, and 6.5 MHz). The values plotted are for the component of the gradient field that is along $B_0$. **b:** The same as **(a)**, but for the Z-gradient coils, plotted along the equi-field lines in the XZ plane.
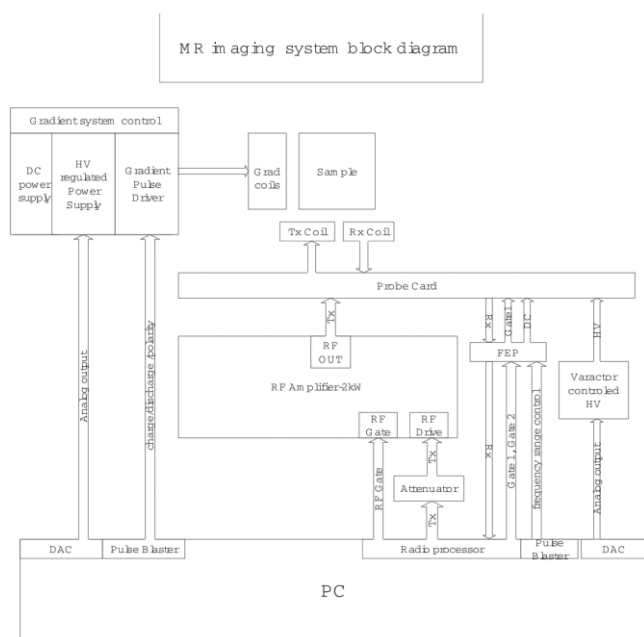
MR imaging system block diagram



FIG. 7. Block diagram of the MRI system.

resistance of 0.8 $\Omega$. Fig. 6b shows the calculated fields generated by the Z-gradient coils along equifield arcs in the XY plane of the probe (from which the signal is obtained, see Fig. 5 for the excited volume geometry in the XY plane). As in the case of the $\phi$-gradient coil, the gradient is not constant along the FOV, but it is still monotonic enough to enable the image acquisition. The average value of the gradient and the image resolution for gradient pulse with a peak current of 50 A and a duration of 30 $\mu$s (half-sin shape) are provided in Table 1. When compared to the $\phi$-gradient coils, the gradient magnitude in most of the FOV does not decrease significantly when moving away from the $\phi = 0$ plane. This is due to the use of three coil pairs which cover effectively the entire FOV along the $\phi$ axis in the $\phi = \pm 45°$ span. Nevertheless, at locations that are close to the probe surface ($< 10$ mm) and for large $\phi$ angles, the gradients can fall by as much as 50% vs the $\phi = 0$ case. This, again, must be and is corrected during image processing (see below).

## Imaging Spectrometer Hardware

The main novelty in this work is related to the unique self-contained MRI module presented above. Nevertheless, a few aspects of the supporting imaging spectrometer hardware are not trivial and warrant separate description (the large bandwidth of operation, the gradient drivers that generate short and strong pulses, and the overall "homemade" spectrometer architecture). Figure 7 shows the block diagram of the entire system. The homemade spectrometer is based on a RadioProcessor PC card (by SpinCore, Gainesville, FL) that generates the RF pulses and receives the NMR signal. This card also generates transistor-transistor logic (TTL) control signals for the power amplifier and acquisition gates for the low-noise amplifier. Another PC card (PulseBlaster by SpinCore),

which is synchronized to the RadioProcessor, generates the rest of the TTL control signals such as signals to the mechanical relay switches and to the gradient drivers unit. The third and final PC card that completes the control system is a digital-to-analog converter (PCI-6733 by National Instruments, Austin, TX) that generates analog voltage to determine the magnitude of the gradient pulses and the varactor diode tuning voltage. Returning to the signal path, after being generated by the RadioProcessor, the RF pulses are amplified by a 2-kW power amplifier (Tomco, Norwood, Australia). Following that, the high power pulses go into the probe card in which the tuning capacitors and the mechanical relay switches are located in close physical proximity to the Tx coil. The NMR signal is then picked up by the Rx coil (which is disconnected during transmission by a PIN diode switch that is located on the probe card). The Rx coil is tuned to the right frequency by a combination of fixed capacitors, selectable through a computer-controlled fast mechanical switch, and a varactor diode (all located on the probe card). The high voltage needed to tune the varactor diode is generated by the "varactor controlled high voltage (HV)" unit. The NMR signal is then amplified by the front-end pod (FEP) unit and returns to the computer for further processing. The gradient drivers can generate currents of up to 50 A for short durations of $\sim 30$ $\mu$s. This is achieved by a variation of the system described elsewhere (24). In this case, we charge a capacitor of $\sim 5$ $\mu$F to voltages of up to 420 V. The shape of the current produced by such system is a half sin (24).

## Imaging Pulse Sequence and Image-Correction Algorithm

The unique geometry and the physical limitations imposed on the design of the probe make it difficult to employ conventional imaging sequences and image processing algorithms. Therefore, we present here the special imaging sequence and image-correction algorithm used in this work.

### Imaging Sequence

The gradient coils for the $\phi$- and Z–axes, as well as the native permanent gradient along the radial axis extending away from the probe (Fig. 3d), are used for 3D spatial encoding of the acquired signal. These gradient coils are used in conjunction with two types of pulse sequences, whose outputs are combined to obtain the image. The first type of sequence is a conventional CPMG multiecho sequence (Fig. 8), where the 90° RF pulse is along the rotating frame X-axis and all the subsequent 180° RF pulses are along the rotating frame Y axis (25). The second type is the Carr-Purcell (CP) multiecho sequence, which is very similar to CPMG but with the phase of the 90° RF pulse set along the Y-axis of the rotating frame. As noted in the past (25), for these types of sequences the NMR echo signal along the echo train is strongly dependent upon the phase of the 90° RF pulse: slowly decaying in a $T_2$ rate for CPMG, and decaying fast for CP. Therefore, in most cases CPMG sequences will be used for imaging. For example, in a "conventional" CPMG-based imaging sequence (such as the rapid acquisition with relaxation enhancement (RARE)
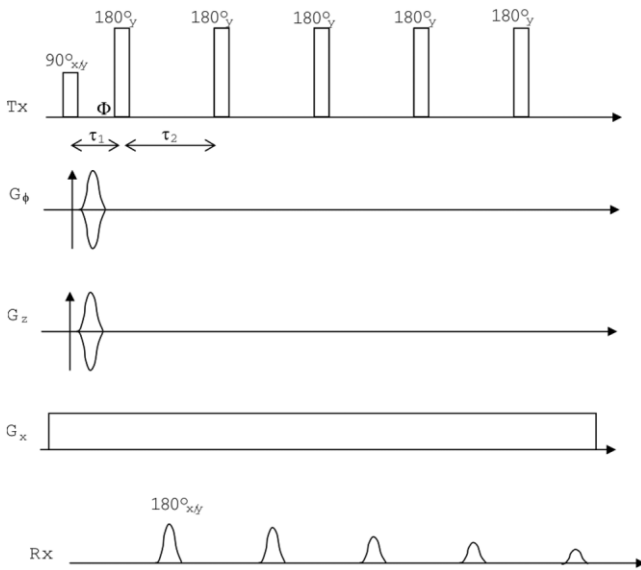
FIG. 8. Imaging pulse sequences for the semitransrectal probe. The pulse field gradient is applied between the first $\pi/2$ and the $\pi$ pulses of the CPMG train. Typically, $\tau$ would be ~50 $\mu$s, $T$ is ~50 ms, and $T_R$ is ~500 ms.

sequence (26)) there is no phase-encoding gradient between the 90° RF pulse and the first 180° RF pulse in order to preserve the phase of the former and obtain a high signal along the entire echo train. Consequently, the overall phase resulting from the encoding gradient between adjacent 180° RF pulses must be zero. This is achieved by applying a positive and then a negative encoding gradient lobe before and after each echo in the train (26). In our system, the use of such an imaging sequence is not practical due to the high currents required by the encoding gradients and the short time between adjacent echoes. Applying such short and intense encoding gradient lobes before and after all the echoes in the train would result in a strong heating effect and would require an extremely high average power out of the gradient drivers. A possible solution to this problem is to apply a single-phase encoding pulse after the 90° RF pulse. However, this approach results in many artifacts, especially for ex situ NMR probes with a very inhomogeneous RF field. These artifacts can be removed by an appropriate phase cycling of the RF pulse sequence to extract an artifact-free signal (11). In this work, we have used a variant of that approach, based on the use of both CPMG and CP in accordance to the following reasoning and signal analysis:

Normally, if one applies a single gradient lobe to encode all the echoes in the train and places it between the 90° RF pulse and the first 180° RF pulse, this violates the required condition for the CPMG sequence since the phase after the 90° RF pulse is not preserved. In order to examine ways to correct that problem, we refer to an analysis of such multiecho pulse sequence (5,27-29). Suppose that the phase of the spins just before the first 180° RF pulse with respect to the phase of the 180° RF pulse is $\mu$, as shown in Fig. 8. According to the analysis (5,27-29), any echo in the train is the sum of an "even parity" echo and an "odd parity" echo. The even-parity echo experiences an even number of

phase inversions by the refocusing RF pulses, while the odd-parity echo experiences an odd number of phase inversions (27). Therefore, the phase of all the even-parity echoes is $\mu$, and the phase of the all the odd-parity echoes is $-\mu$. For the CPMG sequence, where we apply the 90° pulse along the X-axis, the value of $\mu = 0°$ and in the CP sequence case (the 90° pulse along the Y-axis), $\mu = 90°$. In a CPMG sequence (where $\mu = 0$), the even and odd echoes are all in phase and therefore a high signal is maintained along the echo train. In a CP sequence $\mu = 90°$, and thus the even- and odd-parity echoes are out of phase and the signal decreases very quickly along the echo train. When a phase-encoding gradient is applied between the 90° RF pulse and the first 180° RF pulse, the phase $\mu$ becomes spatially dependent, i.e., $\mu = \gamma G_y T$, where $G_y$ is the phase-encoding gradient, $T$ is the duration of the gradient and $y$ is the location along the phase-encoding direction. Naively, one can sum up all echoes along the train for each gradient value and then generate an image by Fourier transform. However, such an image would be the sum of two images based on odd and even echoes, which are encoded by the $\mu$ and $-\mu$ phases, respectively. Thus, a simple Fourier processing would result in considerable image artifacts since the even and odd images (are superimposed together) are reflected along the phase-encoding axis (y in the even image becomes $-y$ in the odd image).

In order to separate the contribution of the even an odd echoes, we employ the algorithm described elsewhere (27). Briefly, each measured echo signal in the train can be processed for any arbitrary $\mu$ to separate its even- and odd-parity echo components by adding and subtracting the signals of the CP and the CPMG sequences. Thus, the entire process is as follows: (1) For each gradient phase-encoding step, the signal for both CP and CPMG sequences is acquired. (2) All the echo train signals are added for the CP and CPMG separately to produce the CP signal and the CPMG signal. (3) Following this the CP and CPMG signals are added and subtracted to obtain the even- and odd-parity echo signals:

$$Even\ parity\ echo\ signal = \frac{CP_{signal} + CPMG_{signal}}{2}$$

$$Odd\ parity\ echo\ signal = \frac{CP_{signal} - CPMG_{signal}}{2} \quad [1]$$

(4) Steps 1-3 are repeated for all phase-encoding steps. (5) The even- and odd-parity echo signals are reconstructed by conventional Fourier analysis to provide the even- and odd-parity images. Since the even- and odd-parity echo signals are all encoded by the same $\mu$ phase, they result in an artifact-free image, denoted by the even (odd) parity image. (6) Both images undergo phase correction. (7) The odd-parity image is reflected along the phase-encoding direction and added to the even image (this improves the SNR by a factor of $\sqrt{2}$). (8) For the case of two orthogonal phase-encoding directions as shown in Fig. 8, the odd-parity image is reflected along both phase-encoding directions and then added to the even-parity image. This algorithm enables us to use the sequence of Fig. 8, despite the violation of the requirement for CPMG echo train.

It should be noted that, for clinical applications, one should consider not only the SNR but also the contrast mechanism between healthy and malignant tissues. Since the probe has a relatively large static gradient, it can be used to obtain both diffusion- and/or $T_2$-weighted images. For example, for a CPMG sequence with restively short $\tau_1$ and $\tau_2$, the summed echo signal is mostly $T_2$-weighted, while for large $\tau_1$ and $\tau_2$, the summed signal is heavily diffusion-weighted (15,16).

*Image-Correction Algorithm*

The probe presented herein has to cover an FOV that is similar to its physical size. This requirement, along with the probe's curved geometry, leads to unavoidable large variations in gradient magnitude throughout the imaging FOV (Fig. 6). Clearly, such variations can lead to large image artifacts and distortions. In order to solve this problem, we have implemented an image-correction algorithm, based on the calculated static and gradient magnetic fields of the probe. The algorithm can be explained as follows.

*One-dimensional image correction.* Suppose one has a one-dimensional image in Y, which is acquired with $N_y$ increments of the phase-encoding gradient $G_y$ followed by a one-dimensional Fourier transform (we use Y instead of $\phi$ axis throughout the reminder of this section for simplicity of writing). For each increment of the phase-encoding gradient, $\Delta G_y$, the phases of the signal from each point on the Y-axis are increased by a vector $\Psi$, which spans from $-\pi$ to $\pi$, having $N_y$ elements with equal increment of $\Delta \Psi = 2\pi/N_y$ radians between adjacent points. For a linear gradient, the constant phase increment $\Delta \Psi$ between each spatial point leads to the reconstructed spatial vector $y$ with constant increment $\Delta y = 2\pi/(\gamma G_y T)$, where $G_y$ is the maximum amplitude of the encoding gradient and $T$ is its duration. For a nonlinear gradient field, the spatial locations on $y$ that correspond to the vector $\Psi$ have unequal increments, and therefore the image after Fourier transform appears distorted.

The $k$th element of the phase vector $\Psi$, $\Psi(k)$, is given by:

$$\Psi(k) = k \cdot \Delta \Psi = \gamma \cdot k \cdot \Delta B(y) \cdot T \qquad [2]$$

where $\Delta B(y)$ is the magnetic field increase at position $y$ due to a single increment of the phase-encoding gradient amplitude, $T$ is the gradient duration, and $\Delta \Psi = 2\pi/N_y$. Since $\Delta B(y)$ depends on $y$, Eq. 2 maps the vector $\Psi$ onto a set of $N_y$ spatial locations $\{y_k\}$ where $k = 1$ to $N_y$. To correct the distorted image, we need to interpolate the image from the locations $\{y_k\}$ into a spatially constant-increment vector that we denote $Y$. In summary, the correction consists of two steps: (a) calculation of the location vector $\{y_k\}$ by numerically solving Eq. 2; (b) interpolation of the image from $\{y_k\}$ into a spatially constant-increment vector $Y$.

*Two-dimensional image correction.* In the case of two-dimensional imaging, the image is acquired with $N_y$ increments of the Y gradient and $N_z$ increments of the Z gradient, followed by a two-dimensional Fourier transformation. The fields of the Y- and Z-gradient coils, $B_y(y,z)$ and $B_z(y,z)$, are known from the field calculations (Fig. 4). After the Fourier transform, the pixels are located on a grid with

equal phase increments. Eq. 2 can be written in the two-dimensional case as follows:

$$\Psi_y(k) = k \cdot \Delta \Psi_y = \gamma \cdot k \cdot \Delta B_y(y,z) \cdot T \qquad [3]$$

$$\Psi_z(m) = m \cdot \Delta \Psi_z = \gamma \cdot m \cdot \Delta B_z(y,z) \cdot T \qquad [4]$$

In this case, the location of equal-phase points is a line and not a single point, as in Eq. 2. Thus, for each $\Psi_y(k)$ in Eq. 3 we have a line of constant phase $L_{y,k}(y, z)$, and for each $\Psi_z(m)$ in Eq. 4, a line of constant phase $L_{z,m}(y, z)$. An arbitrary point $(k, m)$ of our image after two-dimensional Fourier transform ($k = 1..N_y$ and $m = 1..N_z$) is the intersection between these two constant phase lines $L_{y,k}$ and $L_{z,m}$ (which is a single point). The spatial location of this point is denoted $r(k, m)$. Note that $r(k, m)$ has a Y coordinate and a Z coordinate, so $r(k, m)$ consists of two two-dimensional matrices $r_y(k, m)$ and $r_z(k, m)$. The matrices $r(k, m)$ are the spatial locations of the equal-phase image obtained after applying the two-dimensional Fourier transform. To avoid errors due to discretization, we use the fact that $r_y(k, m)$ and $r_z(k, m)$ are slowly varying in space, so that they can be smoothed by fitting to a set of second-order polynomials in two dimensions. Finally, the image is corrected by two-dimensional interpolation of the image from the locations $r(k, m)$ to a constant-grid matrix along Y and Z.

To summarize this algorithm, the spatial correction of the original image (after the Fourier transform) consists of the following steps: (a) for each phase point, $k$ and $m$, calculate the line with constant phase for the Y gradient and the Z gradient and find the intersection between the two lines. The results are the two matrices $r_y(k, m)$ and r$_z$($k$, $m$) with the spatial locations of all the voxels from the original image. (b) Smooth $r_y(k, m)$ and $r_z(k, m)$ by fitting them to two-dimensional polynomials. (c) Interpolate the image to a constant-increment grid in Y and Z. It should be noted that the YZ grid does not coincide with the physical YZ plane of the probe (Fig. 2), but rather corresponds to the (curved) equi. $B_0$ plane for the specific frequency at which the signal is acquired.

## RESULTS

The fully assembled probe was integrated with our NMR system (Fig. 7) and examined to verify its performance. The initial tests included the acquisition of an NMR signal at various frequencies without acquiring an image. The more advanced experiments included image acquisition of test samples.

### NMR Signal

A sample made of agarose gel, which mimics typical tissue NMR parameters ($T_1 = 300$ ms, $T_2 = 100$ ms, at a field of $\sim 5$ MHz), was placed in front of the probe. The NMR signal was acquired by applying a simple CPMG pulse sequence at several frequencies. Due to mechanical reasons the actual position of the probe prototype's Tx/Rx coil, just in front of the magnet, was not as compact as in the original design (see Fig. 10 vs Fig. 2). This made it difficult to acquire a signal at the shorter set of distances
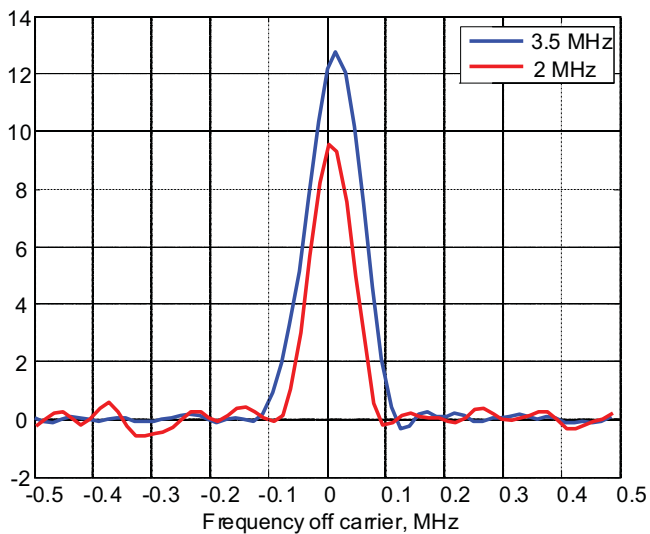
FIG. 9. NMR signal (in the frequency domain) obtained from a large test sample, at 3.5 MHz and 2 MHz.

from the probe. (A clinical probe design would have to include a mechanical solution to this problem that would set the Tx/Rx coil closer to the magnet.) Therefore, the excitation slices that were entirely outside the magnet + Tx/Rx coil structure were only at frequencies below ~3.5 MHz. Fig. 9 shows a typical NMR echo signal obtained at 3.5 MHz and 2 MHz. The signal is the average sum of 250 echoes in the CPMG trains multiplied by 64 scans and four phase cycles (total of $250 \times 64 \times 4 = 64{,}000$ echoes). The measured single-shot SNR was found to be 0.84 and 0.41 at 3.5 MHz and 2 MHz, respectively. This is a bit lower than the predicted values of 1.8 and 0.65, based on the excited-volume NMR simulation (see Table 1 and Fig. 5), but still acceptable considering uncertainties such as magnet and Tx/Rx coil field profiles, line losses, and possible external noise sources.

## Imaging Examples

The probe's imaging capability was evaluated and verified with several test samples. The samples were made of the same agarose gel as the one used for the NMR signal tests. Fig. 10 shows the configuration of the experiments and the
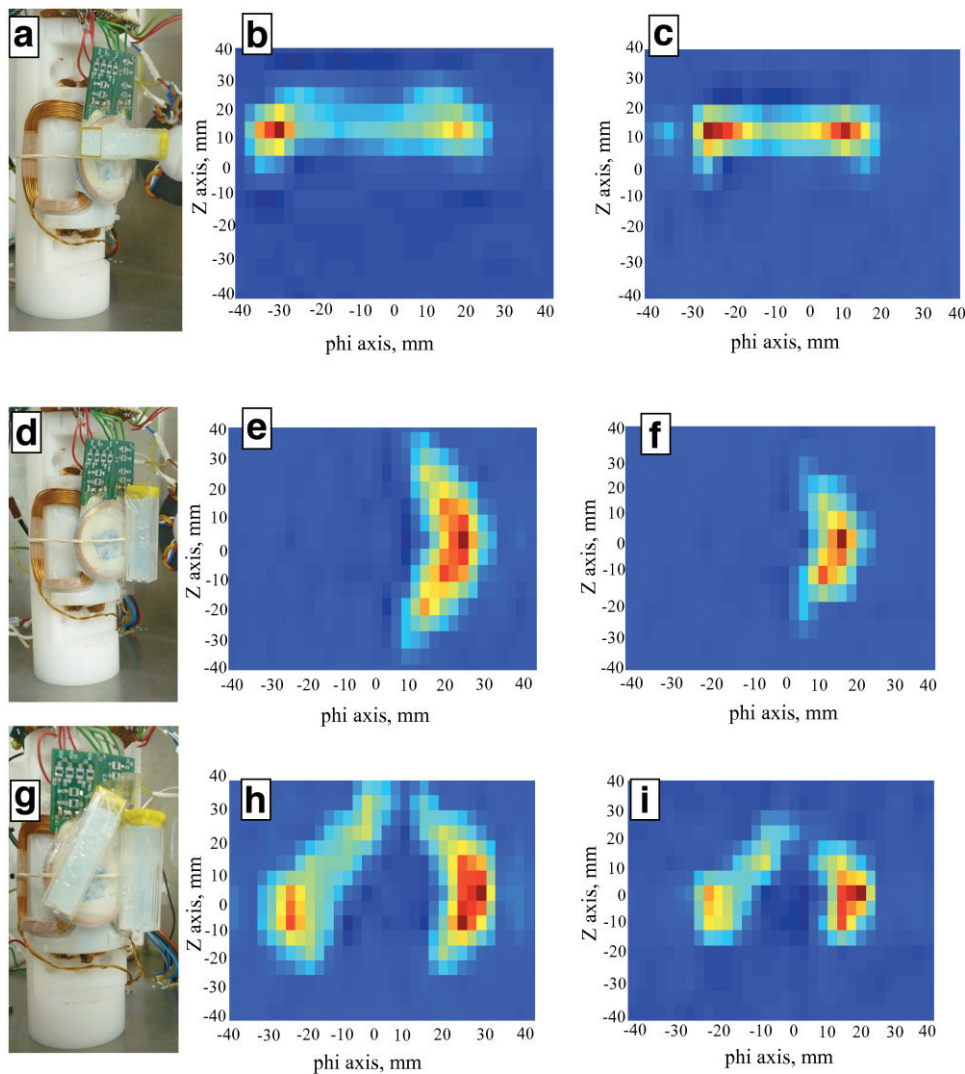


FIG. 10. NMR images of test samples in different configurations. On the left column **(a,d,g)**, we show the experimental setup with the probe and the various agarose gel tubes in different geometrical positions. On the center **(b,e,h)**, the NMR images are presented without any special processing. On the right **(c,f,i)**, the NMR images are shown after processing to correct for the non-linearity and spatial variation of the gradient fields (see section 4.2).

corresponding NMR imaging results. The images were obtained with the following pulse sequence parameters (see Fig. 8): the frequency of operation was 3.4 MHz; the length of both the 90° and the 180° pulses was 10 μs; $\tau_1$ = 82 μs; $\tau_1$ = 140 μs; the echo train included 250 echoes; the duration of the gradient pulses was 30 μs; the sequence was repeated every 300 ms. For the φ-gradient, a current of 20 A was used (~40% of maximum available current), leading to an image resolution of ~5 mm. For the Z-gradient, a current of 40 A was used (~80% of maximum available current), leading to an image resolution of ~11 mm. Thus, the images contain 41 × 41 voxels, with a volume of ~5 × 11 × 1 mm (along the φ, Z, and radial extent of the probe). Image SNR is ~120 and the total acquisition time was ~1 h (performing four-step phase cycling to remove magneto-acoustic ringing and other ring-down noises, and repeating this acquisition for both the CP and CPMG pulse sequences [see section 4.1], a total of 41 × 41 × 4 × 2 = 13,448 trains). The total number of echoes acquired for each image is 250 × 13,448 ~ 3.3 million, leading to single shot voxel SNR of $\sim 120/\sqrt{3.3 \times 10^6}$ = 0.066. If we compare these results to Table 1 (and take into account the image voxel volume), we find that the image SNR is a factor of ~1.8 smaller than one should expect. This relatively minor difference with regard to the theory is similar to what we have found in the case of a "simple" NMR signal without imaging (see section 5.1 above).

## SUMMARY AND CONCLUSIONS

This work has shown for the first time the possibility of acquiring NMR images in an ex situ manner with an FOV that is comparable to the size of the probe. Major challenges such as magnet design, Tx/Rx coil design and construction, wide bandwidth of operation, gradient coil design and construction, gradient drivers, control software, and image processing software were all faced in order to achieve reasonable NMR images of test samples. The probe is envisioned to be useful in several modes of action, based on its final performances and capabilities. The most basic mode of operation of this probe would be biopsy targeting, where the information obtained by the MRI module would only be used to direct the insertion of the biopsy needles to a targeted set of suspected voxels. Urologists tend to ignore lesions that are smaller than ~0.5-1 mL. Therefore, for this type of application, a very moderate MRI image resolution would be sufficient to greatly improve upon the current procedure that is based on "random biopsy" and often requires many needle insertions and leads to repeated procedures (30). Furthermore, in this mode of operation the imaging time (limited by the SNR) can be greatly reduced by co-adding about five voxels along the radial extent of the probe, where the current resolution is relatively high (~ 1 mm). More advanced operation modes, where the probe is to be used for screening and possibly periodic staging, could be pursued later on following some hardware and software improvements that would lead to improved image resolution and reduced acquisition time. These improvements may include, for example (a) using miniature RF mechanical switches based on microelectromechanical systems technology to tune the frequency of

the Rx coil to discrete values with several fixed capacitors, instead of employing the varactor solution (which reduces SNR by a factor of ~2-3); (b) increasing resolution by having a larger gradient strength and employing more efficient schemes for *k*-space coverage; (c) including contrast enhancement in the imaging protocol; and (d) further optimizing the permanent magnet as an independent unit or possibly combing it with an external magnet placed on the patient. Such improvements and others may enable the probe to image a larger portion of the prostate, with a higher resolution and shorter acquisition time. Nevertheless, it is clear that this technology by no means can approach the current state-of-the-art MRI with endorectal coils (reaching submillimeter resolution with a very high SNR). The probe's relative simplicity of operation and low cost inevitably lead to unavoidable compromises in performance that should hopefully still be good enough for several important clinical applications.

Clearly, much work is still needed before a fully clinical probe can be demonstrated. This includes, for example, a better mechanical setup that minimizes the volume taken up by the Tx/Rx coils, improved calculation and even mapping of the gradient coil, which would minimize image artifacts (using the image-correction routines), and further reduction of the acquisition time, employing the means discussed above. Nevertheless, we believe that the work carried out in this project can be considered as a good starting point, providing many answers to difficult feasibility-related issues. Furthermore, it has shown how our detailed theoretical design tools can materialize into a workable probe.

## ACKNOWLEDGMENTS

## REFERENCES

1. Salibi NM, Brown MA. Clinical MR spectroscopy: first principles. New York: Wiley-Liss; 1998. 220 p.
2. Burnett LJ, Jackson JA. Sensitivity of NMR detection for external samples. Bull Am Phys Soc 1980;25:45.
3. Eidmann G, Savelsberg R, Blumler P, Blumich B. The NMR MOUSE, a mobile universal surface explorer. J Magn Reson A 1996;122:104–109.
4. McDonald PJ, Newling B. Stray field magnetic resonance imaging. Rep Prog Physics 1998;61:1441–1493.
5. Hurlimann MD, Griffin DD. Spin dynamics of Carr-Purcell-Meiboom-Gill-like sequences in grossly inhomogeneous $B_0$ and $B_1$ fields and application to NMR well logging. J Magn Reson 2000;143:120–135.
6. Brown RJS, Chandler R, Jackson JA, Kleinberg RL, Miller MN, Paltiel Z, Prammer MG. History of NMR well logging. Concepts Magn Reson 2001;13:335–413.
7. Goelman G, Prammer MG. The CPMG pulse sequence in strong magnetic-field gradients with applications to oil-well logging. J Magn Reson A 1995;113:11–18.
8. Haken R, Blumich B. Anisotropy in tendon investigated in vivo by a portable NMR scanner, the NMR-MOUSE. J Magn Reson 2000;144:195–199.
9. Scharfenecker A, Ardelean I, Kimmich R. Diffusion measurements with the aid of nutation spin echoes appearing after two inhomogeneous radiofrequency pulses in inhomogeneous magnetic fields. J Magn Reson 2001;148:363–366.
10. Perlo J, Casanova F, Blumich B. Ex situ NMR in highly homogeneous fields: H¹ spectroscopy. Science 2007;315:1110–1112.

11. Perlo J, Casanova F, Blumich B. 3D imaging with a single-sided sensor: an open tomograph. J Magn Reson 2004;166:228–235.

12. McDonald PJ. Stray field magnetic resonance imaging. Prog Nuclear Magn Reson Spectrosc 1997;30:69–99.

13. Chao SH, Dougherty WM, Garbini JL, Sidles JA. Nanometer-scale magnetic resonance imaging. Rev Sci Instrum 2004;75:1175–1181.

14. Tsuji S, Masumizu T, Yoshinari Y. Magnetic resonance imaging of isolated single liposome by magnetic resonance force microscopy. J Magn Reson 2004;167:211–220.

15. Blank A, Alexandrowicz G, Muchnik L, Tidhar G, Schneiderman J, Virmani R, Golan E. Miniature self-contained intravascular magnetic resonance (IVMI) probe for clinical applications. Magn Reson Med 2005;54:105–112.

16. Schneiderman J, Wilensky R, Weiss A, Samouha E, Muchnik L, Chen-Zion M, Ilovitch M, Golan E, Blank A, Flugelman M, Rozenman Y, Virmani R. Diagnosis of thin-cap fibroatheromas by a self-contained intravascular magnetic resonance imaging probe in ex vivo human aortas and in situ coronary arteries. J Am Coll Cardiol 2005;45:1961–1969.

17. Wilensky RL, Song HK, Ferrari VA. Role of magnetic resonance and intravascular magnetic resonance in the detection of vulnerable plaques. J Am Coll Cardiol 2006;47:C48–C56.

18. Blumich B, Perlo J, Casanova F. Mobile single-sided NMR. Prog Nuclear Magn Reson Spectrosc 2008;52:197–269.

19. Kirkham APS, Emberton M, Allen C. How good is MRI at detecting and characterising cancer within the prostate? Eur Urol 2006;50:1163–1175.

20. Kleinberg RL, Sezginer A, Griffin DD, Fukuhara M. Novel NMR apparatus for investigating an external sample. J Magn Reson 1992;97:466–485.

21. Paulsen J, Bouchardb L, Graziania D, Blumich B, Pines A. Volume-selective magnetic resonance imaging using an adjustable, single-sided, portable sensor. Proc Natl Acad Sci U|S|A 2008;105:20601–20604.

22. Cook B, Lowe IJ. A large-inductance, high-frequency, high-Q, series-tuned coil for NMR. J Magn Reson 1982;49:346–349.

23. Zur Y. An algorithm to calculate the NMR signal of a multi spin-echo sequence with relaxation and spin-diffusion. J Magn Reson 2004;171:97–106.

24. Conradi MS, Garroway AN, Cory DG, Miller JB. Generation of short, intense gradient pulses. J Magn Reson 1991;94:370–375.

25. Meiboom S, Gill D. Modified spin-echo method for measuring nuclear relaxation times. Rev Sci Instrum 1958;29:688–691.

26. Hennig J, Nauerth A, Friedburg H. Rare imaging: a fast imaging method for clinical MR. Magn Reson Med 1986;3:823-833.

27. Zur Y, Stokar S. A phase-cycling technique for cancelling spurious echoes in NMR imaging. J Magn Reson 1987;71:212–228.

28. Norris DG, Bornert P, Reese T, Leibfritz D. On the application of ultra-fast rare experiments. Magn Reson Med 1992;27:142–164.

29. Norris DG. Selective parity RARE imaging. Magn Reson Med 2007;58:643–649.

30. Shinohara K. Improving cancer detection by prostate biopsy: the role of core number and site: commentary. Nat Clin Pract Urol 2006;3:526–527.